Journal of Catalysis **185,** 286–296 (1999)
Article ID jcat.1999.2509, available online at http://www.idealibrary.com on IDEAL®

Catalyzed Carbon–NO Reaction Studied by Scanning Tunneling Microscopy and *ab Initio* Molecular Orbital Calculations

Helen Y. Huang and Ralph T. Yang[1]

Department of Chemical Engineering, University of Michigan, Ann Arbor, Michigan 48109-2136

Received September 8, 1998; revised October 3, 1998; accepted March 30, 1999

The STM technique has been employed to study the catalysis of the carbon–NO reaction by alkali, alkaline earth, and transition metal catalysts. The catalytic actions by the catalysts used in this study follow the well established modes of channeling, edge recession, and pitting. The turnover frequencies of the catalyzed reactions are calculated based on the channeling rates on the basal plane of graphite with 1% NO at 600°C, and the relative catalytic activities of the catalysts are compared. NO is dissociatively chemisorbed by these catalysts, followed by diffusion of O atoms to the edge carbon sites, where breakage of C–C bonds takes place to free CO. The rate-limiting step for the gasification reaction by NO is the breakage of C–C bonds. *Ab initio* **molecular orbital calculations are performed on model graphite substrates with –O and –O–*M* groups (where *M* = metal) bonded to the zigzag face. The surface C–C bonds in these structures are substantially weakened by adding –O or –O–*M* on the active carbon atom, leading to CO release. The extent of weakening in the C–C bond energy by different metals is in general agreement with the order of catalyst activities measured as turnover frequencies. The rank order of TOF by different catalysts is Cu > Ba = K > Sr > Ca > Mg > Na > Co > Fe = Li.**

INTRODUCTION

The C + NO reaction is the least understood reaction among all gas–carbon reactions. Yet it is important due to its environmental ramifications. The catalyzed C + NO reaction is receiving increasing attention because (i) it is a significant reaction in combustion systems and (ii) it is considered a possible means for NO reduction (1–8). Alkali, alkaline earth, and transition metals are among the best known catalysts for the C + NO reaction as well as the other gasification reactions of carbon. A large volume of literature has been devoted to the understanding of these catalyzed reactions (9–22).

The key to the understanding of the gas–carbon reaction lies in the active surface complexes, and the surface oxygen complexes play a dominant role in the reaction involving oxygen-containing gases. A generally postulated mechanism (23–27) consists of the oxidation–reduction cycle in which oxygen is transferred to the carbon active sites through the catalytically active metal species, followed by breakage of the neighboring C–C bonds and the release of CO from the carbon structure. The last step is considered as the rate-limiting step. This mechanism accounts for many experimental results (28–33) even though the active intermediates are not well understood.

Various intermediates have been proposed for different catalysts (34–38). For example, the proposed intermediates for potassium catalysts include metallic K (39), K_2O (39–41), K_2O_2 (42), K_2CO_3 (39, 40), and C–O–K (43–49). Of these active intermediates, the C–O–K type group has received much attention. This surface group is an activated and stable group which facilitates a high dispersion of the catalyst. Evidence for the existence of this group and its role in the carbon gasification reaction have been shown and discussed by many researchers (43–47). More recently, the C–O–K group is suggested as the anchor through which catalyst clusters are attached to the edge carbon sites (32). It has become evident that the phenolate (C–O–M) groups do exist and are active for the catalytic carbon gasification reaction.

A unique and most intriguing phenomenon associated with the catalyzed gas–graphite reaction is the motion of the catalyst on graphite which results in the catalytic activity. This phenomenon has been revealed and studied on the basal plane of graphite single crystals, using controlled-atmosphere TEM (50–52) and etch-decoration TEM (36, 53–55). A number of catalyst motions have been observed. These include pitting (34, 56), deep channeling (9, 38, 50), and deep edge recession (57, 58). It has been established, primarily by Baker and coworkers (59) using controlled-atmosphere TEM, that the catalyst acts mainly by carving channels in graphite and coating edges at the graphite layers to promote edge recession. All channels initiate at the steps and edges. The dominant mode of catalyst action depends on the wetting between the catalyst and the carbon edges, which in turn depends on the gas environment and temperature. The catalytic actions are propagated by

[1] To whom correspondence should be addressed. Fax: (734) 763-0459. E-mail: yang@umich.edu.

0021-9517/99 $30.00

adhesion forces; the catalyst is active when it wets the graphite edges.

The controlled-atmosphere TEM technique, however, relies on the relative contrast of images which requires channels many graphite layers deep (e.g., >30 layers) and consequently "overlooks" catalytic events occurring on the surface layers of graphite. By using etch-decoration TEM, monolayer channeling has been discovered (17–21).

Recently, scanning tunneling microscopy (STM), a very powerful tool for studying the structure and physical properties of conducting and semiconducting solid surfaces (60, 61) has been employed to study the uncatalyzed or catalyzed gasification reactions of graphite (62–66). In STM, a tunneling current is produced when an anatomically sharp tip is brought close to the sample surface. The tunneling is confined to a very small area and the current is sensitive only to the local surface features. This makes it capable of imaging the sample surface with atomic resolution (67). Another important feature of STM is its ability to image nonperiodic or disordered surfaces (68). This is particularly useful for studying catalytic gasification reactions of graphite, where the basal plane of graphite is carved by catalyst particles in shallow or multilayer pits and channels.

An interesting problem concerning catalyzed carbon gasification is the relative catalytic activities of different metal compounds in the same reaction atmosphere. In this work, the catalyzed carbon–NO reaction is studied by the STM technique using a highly oriented pyrolytic graphite (HOPG) and alkali, alkaline earth, and transition metal oxides as the catalysts. The aim of this work was to characterize the different pits and channels created on the surface of graphite by the catalysts and to study the relative catalyst activities. It is also our goal to study the reaction mechanism of the catalyzed carbon–NO reactions. An *ab initio* molecular orbital calculation is performed in order to provide a better understanding of the origin of the catalytic activity for the carbon–NO reaction.

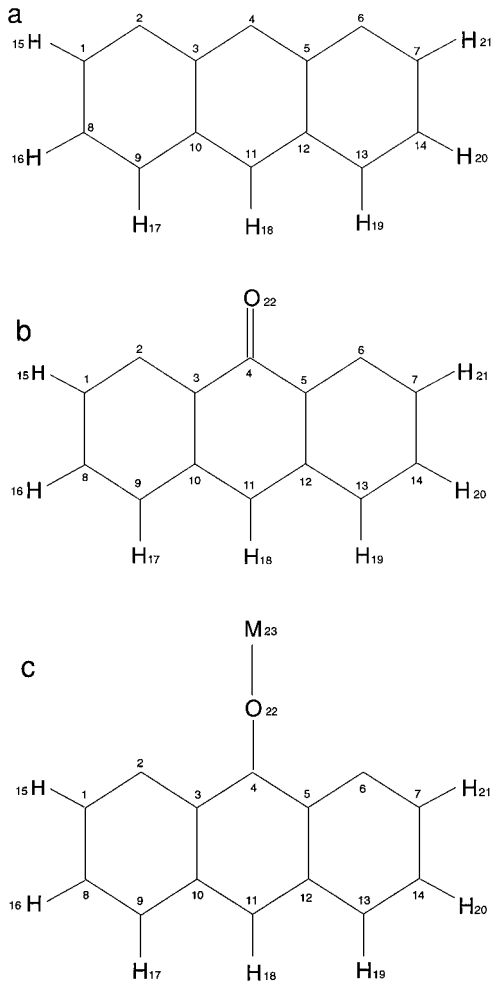

FIG. 1. Graphite models for molecular orbital calculations. (a) Model with hydrogen saturating the edge carbon sites, (b) model of chemisorbed oxygen on active site, (c) model with –O–*M* group attached on the active site (*M* = metal).

AB INITIO MOLECULAR ORBITAL CALCULATION

Molecular orbital calculation has been proven to be of great utility in our understanding of chemical bonding and other chemical phenomena. It has been used to study chemisorption on graphite surfaces (69–72). In this work, the Gaussian 94 package (73) was used for all *ab initio* calculations.

The graphite models used in the calculation are shown in Fig. 1. Figure 1a is the substrate for the zigzag edge of graphite; Fig. 1b is the model for the semiquinone intermediate; Fig. 1c is the graphite substrate with a phenolate group (–O–*M*, where *M* is metal). Only zigzag edges of graphite are considered here because it has been previously shown that the C–C bonds are stronger on zigzag edges, and hence the breakage of these bonds is rate-limiting (11, 12, 71). In order to minimize the edge effect, hydrogen atoms are used to saturate the edge site carbons (except the edge site carbon for reaction). Although there are many methods of terminating the boundaries, the use of hydrogen remains to be the best choice in consideration of both charge balance and chemical environment (13, 69).

Prior to bond energy calculation, the unrestricted Hartree Fock (UHF) theory at the STO-3G level basis set was used to optimize the geometry of each of the models shown in Fig. 1. The optimized structures were then used to calculate the SCF energies at a higher level, B3LYP/3-21G. The reason for choosing the minimum basis set for geometry optimization is twofold. First, it is known that the computational cost of the all-electron *ab initio* calculations increases as N^4, where N is the number of electrons. With a large calculation model like $C_{14}H_7OM$ used in this study, it will be too costly to use a larger basis set for geometry

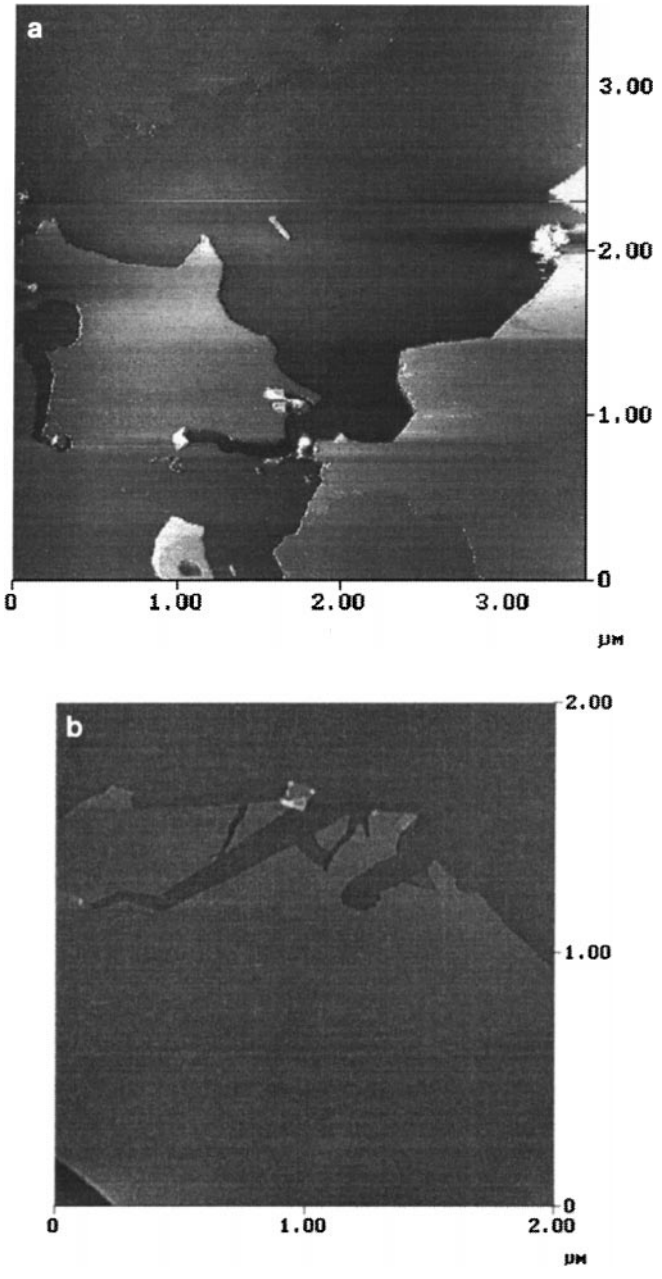

FIG. 2. STM image showing two types of channeling actions by Li on the basal plane of graphite after exposure to 1% NO at 600°C for 90 min. (a) Constant-width channeling (channel depth, 2.0 nm). (b) Flute shape channeling (channel depth, 0.67 nm).

optimization. Second, a traditional and most reasonable way for predicting the total energy of a system is to "perform a low-level geometry optimization and run a higher level single point energy calculation at the optimized structure" (73). Moreover, energies computed with the B3LYP functional are surprisingly insensitive to the geometry optimization level (73). The method that we use for comparison of relative catalytic activities by different catalysts is on the same basis.

Bond energy is not available in most molecular orbital calculation packages including Gaussian 94. In our previous work (13), we used the method of breaking the molecular system of interest into several pieces at the C–C bond and calculating the C–C bond "dissociation" energy accordingly. However, when the molecular system was broken down, the chemical environment was changed and this might result in errors in the energy calculation. In this work, we used a better procedure in bond energy calculation as described in the following steps:

Step 1. Optimize the geometries of the structures shown in Fig. 1. Then perform single point total SCF energy calculation at each of the optimized structures.

Step 2. For a geometrically optimized structure, we change equally (increase or decrease) the bond length of the two C–C bonds of interest (C_3–C_4 and C_4–C_5 as shown in Fig. 1). Consequently, the system energy increases as the C–C bond length changes because the molecular structure moves away from its geometrically optimized position, which represents the minimum on the potential energy surface.

Step 3. Repeat step 2 until there is no further change in the total energy upon change in the C–C bond length. At this point, the total energy reaches the level where the two C–C bonds are thoroughly dissociated from the substrate. The C–C bond energy is thus obtained from the energy vs. bond length curves, as the difference between the minimum and this level.

Since the bond energies of the C_3–C_4 and C_4–C_5 bonds are not distinguishable, we simply divide the total bond energy by two and assume the final bond energy to be the C–C bond energy in the graphite model under consideration.

EXPERIMENTAL

The carbon used in this study was highly oriented pyrolytic graphite (HOPG) from Union Carbide. This graphite was chosen for its well-defined structure and an easily prepared, atomically flat surface. Another importantly feature is its high purity since it is our goal to avoid any involvement of catalytic effect caused by impurities in the sample. Details of HOPG are given elsewhere (74). Ultrahigh-purity helium with a minimum purity of 99.999% (from Matheson) was used as the inert carrier gas and was subjected to further purification to remove traces of O_2 by passing through copper turnings at 550°C, since the presence of O_2 would enhance the graphite etch rates.

Ten catalysts (Li, Na, K; Mg, Ca, Sr, Ba; and Fe, Co, Cu) were studied. The catalysts were dispersed on the basal plane of graphite from 1.0 N nitrate solutions. At our reaction temperature of 600°C, all the catalyst precursors, nitrate compounds, should have been decomposed to form oxides. So the catalyst particles were metal oxides.

However, since the reactant contained 1% NO, some nitrites could be formed depending on the thermodynamic equilibria with the metal oxides. Before dispersing catalyst particles on the basal plane of graphite, the graphite sample was cut and cleaved into small and thin pieces (to be fitted in the STM). The small HOPG pieces were further peeled with Scotch tape to expose the fresh surface. Then the sample was placed on a filter paper, on which the solution was dispersed. After air drying, the catalysts were dispersed on the basal plane as confirmed by microscopy. The graphite sample containing catalyst was placed on a sapphire plate that was held in an alumina combustion boat (36). The boat was placed in a quartz tube furnace. Prior to the reaction, the graphite basal plane was degassed overnight in helium at 500°C (36). After degassing, the temperature was raised to the reaction temperature of 600°C and the gas was switched to the reactant (mixture of 1% NO and 99% He). After 90 min of reaction, the reaction gases were switched back to helium and the temperature was allowed to drop to room temperature.

The STM experiments were carried out on a NanoScope III scanning probe microscope (from Digital Instruments) at 300 K in air. The tungsten tips were obtained by electrochemical etching of the cut tungsten wire at 10 V constant voltage with 1.0 N NaOH as the etching solution. The constant current mode was used for all images with scanning rates adjusted for the best images. Other scanning parameters were integral gain, 3.0; proportional gain, 2.0; setpoint, 2.0 nA; and bias, 2.00 V. The surfaces were first randomly imaged in a large $40 \times 40\ \mu m^2$ area for about 10 different regions on each sample. Those showing interesting features were closely scanned with lower Z ranges and slower scan rates to obtain clear images with high resolutions. All images presented were flattened (i.e., digitally treated to remove tilt in the sample relative to the tip-scanning plane) and some large-scale images were filtered by lowpass filtering for higher resolutions. Care was taken to ensure that no information was lost during filtering of the images. The STM images presented in this paper are representative of numerous images measured on different areas of the reacted HOPG surfaces.

RESULTS AND DISCUSSION

Alkali Metal-Catalyzed Graphite–NO Reaction

The alkali metal catalysts (Li, Na, and K) showed the same actions on the basal plane of graphite in NO. The common catalyst actions were multilayer channeling and edge recession. The deep channels all originated from multilayer steps and edges of the graphite. Unlike our previous work (17–21) using single-crystal graphite (from Ticonderoga, New York), no monolayer etch pits and monolayer channels were found on the graphite basal plane. Using STM, Chu and coworkers (64) also observed mostly multilayer channels on HOPG during catalytic gasification reactions. This was due to the different crystal structures of these two kinds of graphite. The HOPG used in this study consisted of small crystals joined together at an average "mosaic spread angle" of 2°; i.e., the average angle of alignment at boundaries was 2°. These boundaries were formed by joining multilayer edges of two or more single crystals. Multilayer channels were initiated from these boundaries. In contrast, the single crystals used in our previous work (17–21) contained no boundaries, but had many vacancies. Monolayer channels and pits were initiated from these vacancies (17–21).

Shown in Figs. 2a and 2b are two STM pictures of lithium catalyzed graphite basal plane after reaction with 1% NO at 600°C for 90 min. The two pictures were taken at different areas of the graphite sample, but both showed channels of about the same length (1.0 μm) despite differences in depth (2 nm vs 0.67 nm). The channel length did not depend on the channel depth. This is consistent with our previous TEM results showing that the C–C bond breakage at the graphite edge-catalyst interface was the rate-limiting step in alkali catalyzed monolayer channeling (11).

Two types of multilayer channels were observed on the graphite basal plane catalyzed by lithium. The first type had nearly uniform width and was generated by a large catalyst particle initiated on a multilayer step. Such action is illustrated by the STM picture shown in Fig. 2a, where a large catalyst particle remained at the leading edge of the channel. Another type of multilayer channels were those with a fluted shape which were usually the result of smaller active catalyst particles coated on the channel walls. Thus only very small and sometimes no catalyst particles could be observed at the leading edge of the channels. Exhibited in Fig. 2b is a typical fluted shape double-layer (two layers deep) channel with a tiny catalyst particle at its leading edge. Two possible reasons for the gradual disappearance of channeling particles have been suggested (75). First, the catalyst particles may evaporate from the surface; and second, the catalyst particles may enter between the graphite layers. Due to the low melting points of the alkali metal compounds, it is most likely that these catalyst particles would exhibit liquid-like behavior at 600°C in NO and they either evaporated or coated on the channel wall.

It is obvious that the channels in Figs. 2a and 2b were initiated from particles of different sizes. However, they showed the same length, i.e., the same channeling rate. Geothel and Yang (18) have discussed in detail the rationale for determining the different rate-limiting steps based on the dependence of channeling rate on the particle size of the catalyst. The results of the lithium catalyzed graphite-NO reaction showed a lack of dependence of the channeling rate on the particle size. The independence of channeling rate on particle size indicates that the rate-limiting step was the breakage of C–C bonds at the carbon-catalyst interface. This

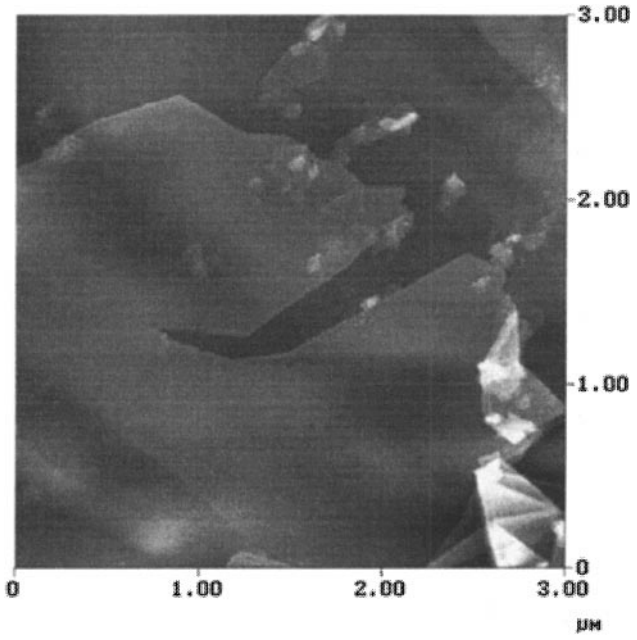

FIG. 3. STM image showing the channeling action of Na catalyst on the graphite basal plane after exposure to 1% NO at 600°C for 90 min.

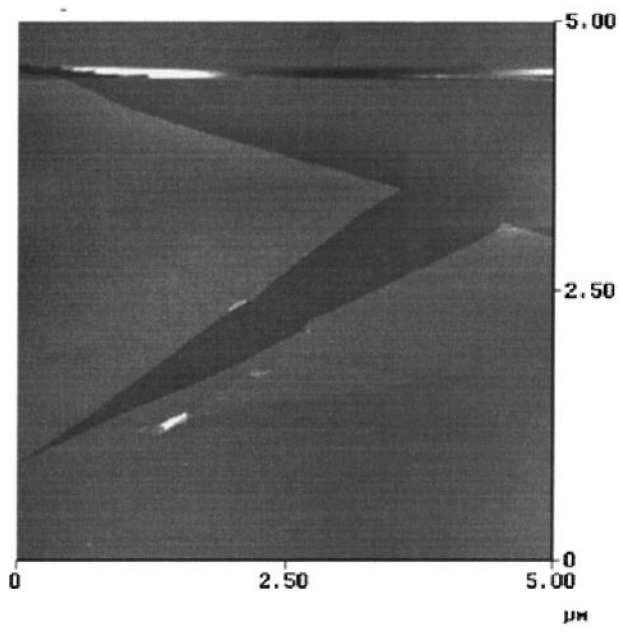

FIG. 4. STM image showing the channeling action of K catalyst on the graphite basal plane after exposure to 1% NO at 600°C for 90 min. The upper (dark) region is five layers below the lower region.

conclusion is in agreement with the conclusion obtained from bulk carbon studies. Isotope exchange experiments (21, 22, 28, 31) showed that oxygen exchanges between the gas reactant molecules and alkali metal catalyst were much faster than the carbon gasification rates, hence the C–C bond breakage was the rate-limiting step.

Channeling by the other two alkali catalysts, Na and K, exhibited similar behaviors, except their different rates as will be explained shortly. Both modes of attack, edge recession and channeling, occurred simultaneously during the reaction. Figures 3 and 4 show STM pictures of the basal plane after the Na and K catalyzed NO-graphite reactions. Figure 4 also gives a clear picture of edge recession in which the upper region in the picture was five layers below the lower region of the picture, and a flute shaped channel was initiated from the edge.

Alkaline Earth-Catalyzed Graphite–NO Reaction

Four alkaline earth metal catalysts (Mg, Ca, Sr, and Ba) were studied under the same reaction conditions as those of the alkali metal catalyzed reactions. Similar to the alkali metal catalyzed C–NO reaction, channeling actions were also found on all of the four alkaline earth catalysts, shown in Figs. 5 through 8. However, multilayer pits were also seen on all of the alkaline earth catalyzed graphite samples.

Two STM pictures showing the typical pitting action by the alkaline earth catalyst are shown in Figs. 7b and 8. A deep layer hexagonal pit was found on the sample with Sr catalyst as shown in Fig. 7b. The depth profile showed that the depth of the pit was 3.72 nm, i.e., about 11 graphite layers, and the width of the pit was about 3 μm. As can be observed from the picture, there were still some bright catalyst particles around the big hexagonal pit. The pit was hexagonal, possibly bounded by armchair faces because these faces were inhibited and thus limiting the growth rate according to our previous TEM and molecular orbital calculation results (11).

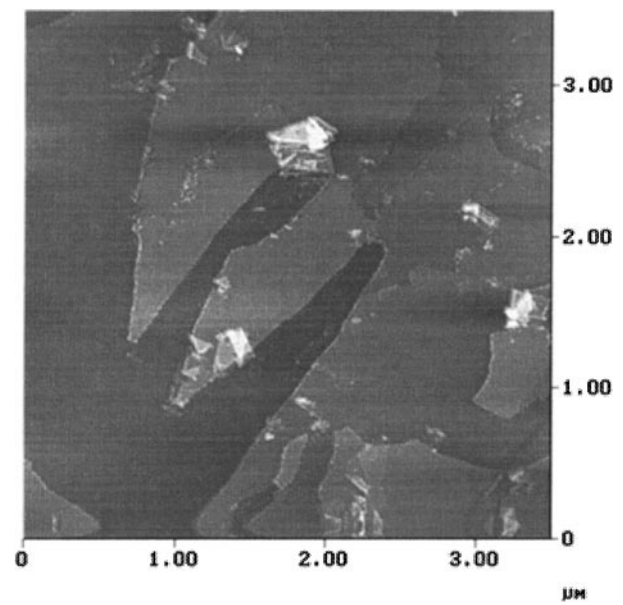

FIG. 5. STM image showing the channeling action of Mg catalyst on the graphite basal plane after exposure to 1% NO at 600°C for 90 min.

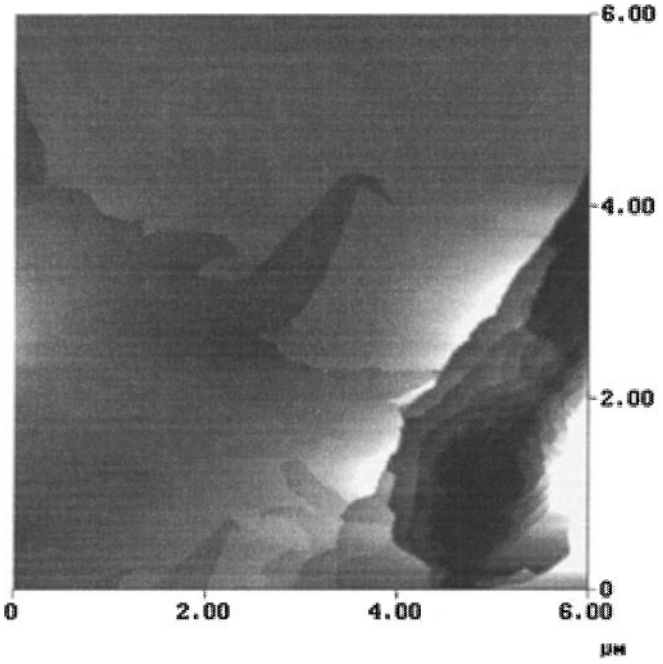

FIG. 6. STM image showing channeling action of Ca catalyst on the graphite basal plane after exposure to 1% NO at 600°C for 90 min.

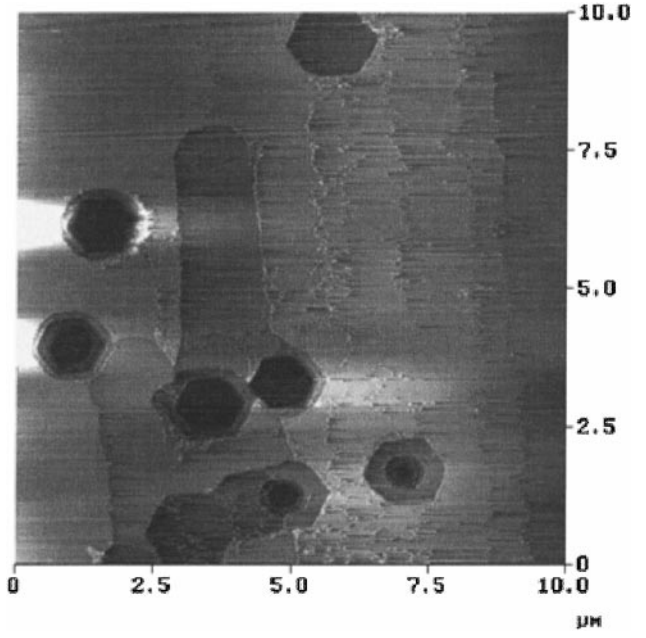

FIG. 8. STM image showing channeling and deep layer pitting (pit depth, 2–48 nm) actions of Ba catalyst on the graphite basal plane after exposure to 1% NO at 600°C for 90 min.

Pitting reactions were even more severe on the Ba catalyzed graphite sample. As shown in Fig. 8, on the $10 \times 10\ \mu m^2$ area, there are nine uniform deep-layer pits with the depth varying from 2 to 48 nm. The initial pits were expanded by edge recession to produce hexagonal-shaped pits. As the reaction continued, the pits became progressively circular in shape.

Transition Metal-Catalyzed Graphite-NO Reaction

Reactions of transition metal catalysts with graphite also showed both channeling and pitting phenomena. The main features of the channeling were essentially the same as those catalyzed by alkali and alkaline earth catalysts as shown in Figs. 9 through 11. Two STM pictures showing the channeling and pitting actions on the Fe catalyzed graphite basal

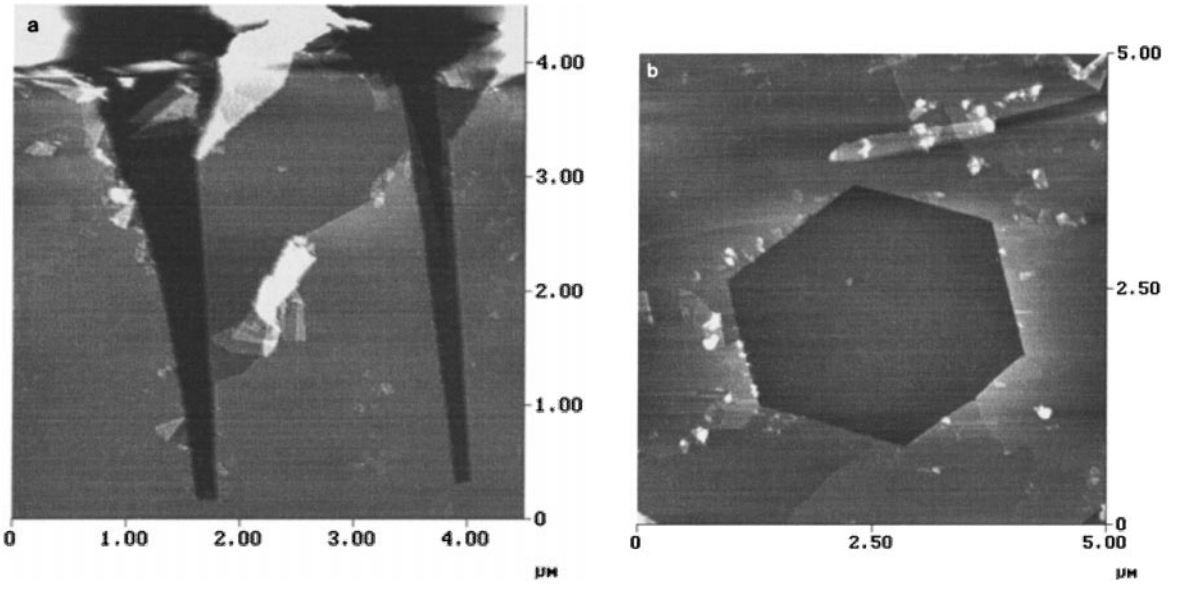

FIG. 7. STM image showing (a) channeling and (b) hexagonal pitting action of Sr catalyst on the graphite basal plane after exposure to 1% NO at 600°C for 90 min. The hexagonal pit in (b) is 3.72 nm or 11 layers deep.

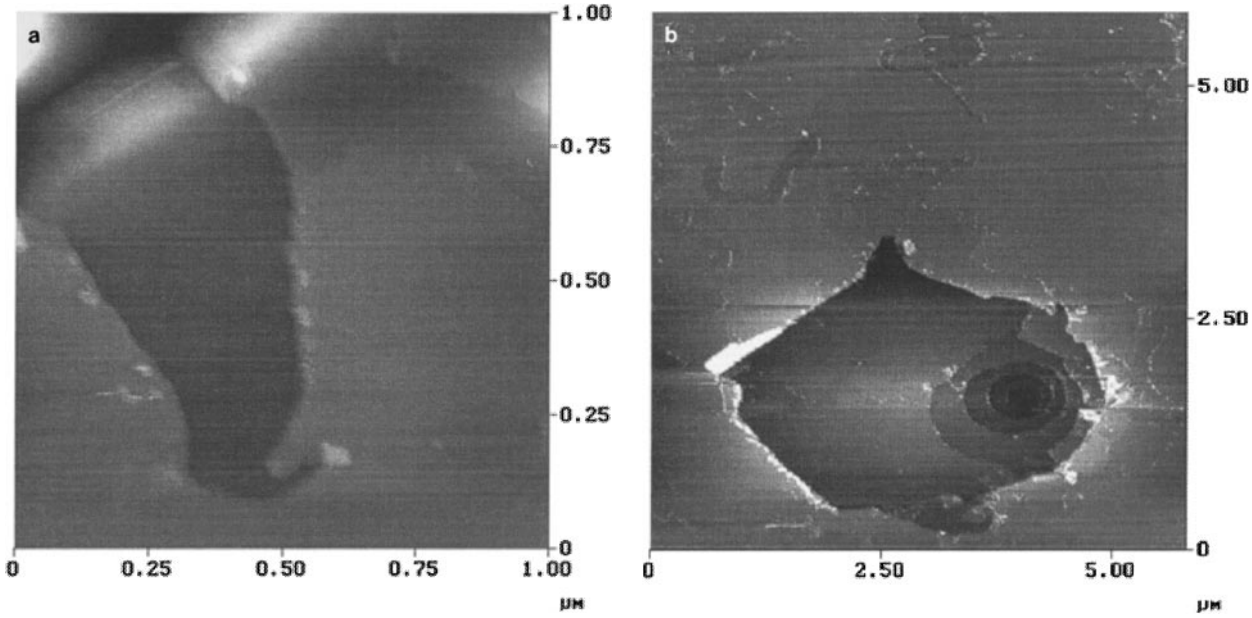

FIG. 9. STM image showing (a) channeling (depth, 2.32 nm or 7 layers) and (b) deep layer pitting actions of Fe catalyst on the graphite basal plane after exposure to 1% NO at 600°C for 90 min. (b) also shows shallow channels (depth, 0.7 nm).

plane are shown in Figs. 9a and 9b. Both flute-shape channels and constant-width channels were observed. From the section analysis of STM, the channel in Fig. 9a was 2.32 nm in depth, i.e., about seven graphite layers deep. The channel shown in Fig. 9b had a uniform depth of about 0.7 nm (i.e., two layers), and despite the difference in the channel depth with that in Fig. 9a, they had almost the same channel length of about 1.25–1.5 μm. Again the lack of dependence of the rate of channeling on channeling depth indicated that the C–C bond breakage was the limiting step for the gasification reaction. Also shown in Fig. 9b is a large multilayer pit. Except for the first layer, the pits were concentric and did not have a perfect circular shape, but they were generally rounded. It appears that the first layer of the pit was

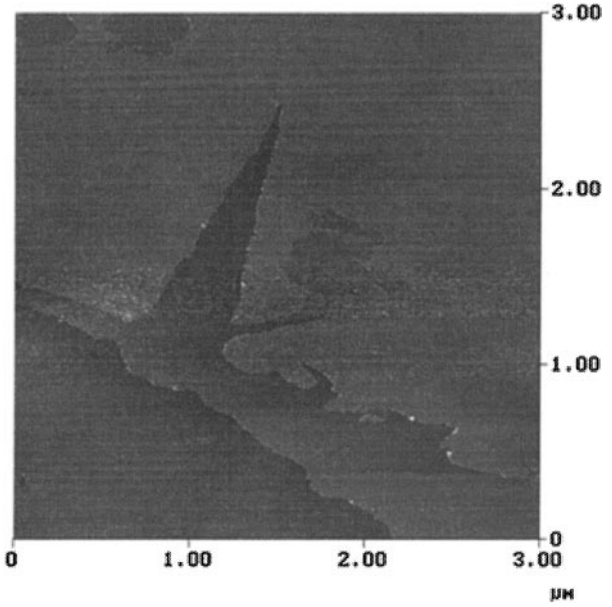

FIG. 10. STM image showing channeling and edge recession of Co catalyst on the graphite basal plane after exposure to 1% NO at 600°C for 90 min. Three planes vary in heights by two layers each.

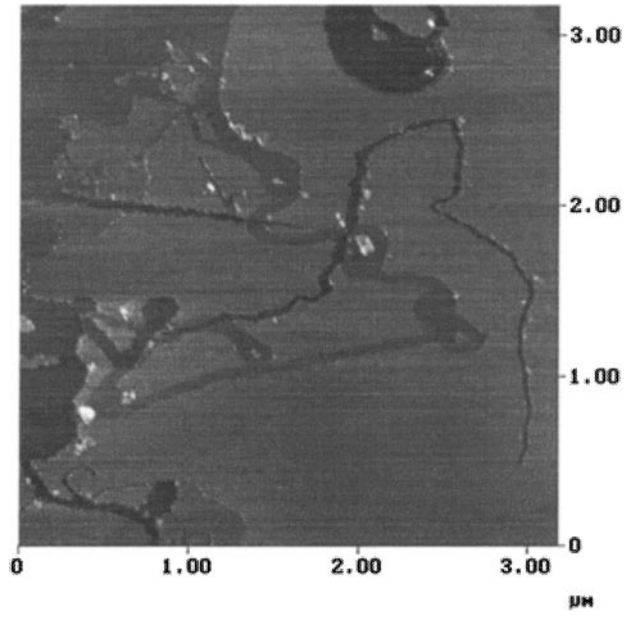

FIG. 11. STM image showing the fast channeling action of Cu catalyst on the graphite basal plane after exposure to 1% NO at 600°C for 90 min.

initiated by catalyst wetting. The catalyst would disperse to coat on the monolayer edges of the pit in the first layer, causing both edge recession and channeling, hence the irregular shape. The second and other lower layers of the pit grew at slower rates because they were formed later and also they had less or no catalyst on the edge. It is expected that there is a high concentration of oxygen atoms within the inner layers of the pit. The oxygen atoms generate new vacancies and a new pit within the first layer. The process repeats itself and successive inner layers were thus formed.

The channeling and edge recession actions of Co catalyst on the graphite basal plane can be seen from Fig. 10. Besides channeling, vigorous edge recession took place on the graphite basal plane. Three planes of different depths can been seen. The depth profile showed that each lower plane was two graphite layers below the planes above it.

Reactions of graphite with NO catalyzed by Cu were found to be extremely fast. A feature unique to the Cu catalyzed graphite–NO reaction was the formation of very narrow and long channels as shown in Fig. 11. Both straight and randomly oriented channels were seen.

The high channeling speed by Cu indicated that Cu was a most active catalyst for the C + NO reaction. It is interesting to note that Cu is also a most active catalyst for $C + O_2$ reaction (e.g., 9, 10). The narrow channels indicated a high dispersion of Cu forming fine particles.

As noted earlier, no deep pitting was observed with the alkali catalysts. Deep pitting was prevalent with alkaline earth and transition metal catalysts. Deep pitting requires formation of oxygen atoms (which create new vacancies on the basal plane). Hence the above result indicates that the alkaline earth and transition metal catalysts are also good catalysts for NO dissociation. The dissociation constants of NO (forming $N_2O + O$), O_2, CO_2, and H_2O have been compared (76). The dissociation constants at 600°C were 10^{-11} for NO and 10^{-23} for O_2, CO_2, and H_2O. The relatively high dissociation constant of NO is the reason for the vigorous pitting for the C + NO reaction. For channeling, wetting is important. The melting points of the alkali catalysts are generally lower than those of the alkaline earth and transition metal catalysts. This may also be a reason for the dominance by channeling for the alkali catalysts.

Turnover Frequencies

The turnover frequency for the catalyzed reaction could be calculated from the channeling rate (17–21). Only channels with both ends well defined were used because not all channels were initiated from the start of the reaction.

By measuring the lengths of the channels which had both clearly defined beginnings and ends and assuming that all channels were initiated at time zero, i.e., when NO was introduced, the rates were calculated. Here the rates were expressed as turnover frequencies based on the active sites of carbon. The active sites were clearly defined, since they were located at the front leading edge of the catalyst particle. The turnover frequencies (in C atom/C atom site/s) for the different catalysts are listed in Table 1. The channeling rates were reasonably uniform from particle to particle, and had error limits within ±0.1 1/s. As we can see from the table, the most active catalyst was Cu and the activities follow the rank order: Cu > Ba = K > Sr > Ca > Mg > Na > Co > Fe = Li.

TABLE 1

The Channeling Turnover Frequencies for the C + NO Reaction by Different Catalysts by 1% NO at 600°C and 1 atm, with Error Limits ±0.1 1/s

Catalyst	Li	Na	K	Mg	Ca	Sr	Ba	Fe	Co	Cu
TOF (1/s)	0.8	1.4	3.8	1.5	1.7	2.8	3.8	0.8	1.1	4.5

The fact that all the alkali, alkaline earth, and transition metal catalysts began to exhibit appreciable channeling activities at the same temperature suggests that the same reaction pathway was followed (12).

The following sequential steps are generally involved in deep channeling as well as monolayer channeling actions during the gasification reactions of carbon (18): (i) chemisorption and reaction of gas molecule (O_2, CO_2, H_2O, or NO_x) at the catalyst–gas interface; (ii) transport (diffusion) of oxygen atoms/ions through or over the catalyst particle to the catalyst–carbon interface to form bonding with the edge carbon atoms; and (iii) breakage of carbon–carbon bonds to free the edge carbon to release CO. For deep channeling in the graphite–oxygen reaction, Baker *et al.* (77) showed that the speed of channeling is inversely proportional to the catalyst particle size, indicating that diffusion of carbon through the catalyst particle is the rate-limiting step. In our study of carbon-NO reaction, as stated previously, there was no dependence between the particle size and channeling speed. A reasonable conclusion is that the breakage of the carbon–carbon bonds is the rate-limiting step; the breakage occurs at the graphite monolayer or multilayer step (where the edge carbon atom has an unpaired sp^2 electron) by the influence of the catalyst.

Ab Initio Molecular Orbital Calculation Results

After full geometry optimization, i.e., all geometry parameters were allowed to change during the optimization, each of the structures reached a minimum on the potential energy surface. The optimized parameters for the graphite models were very close to that of experimental data with deviations less than 0.5%. All the dihedral angles were either 0° or 180°, indicating that the planar structures of graphite were maintained. The analysis of geometry parameters for each individual model was not meaningful since

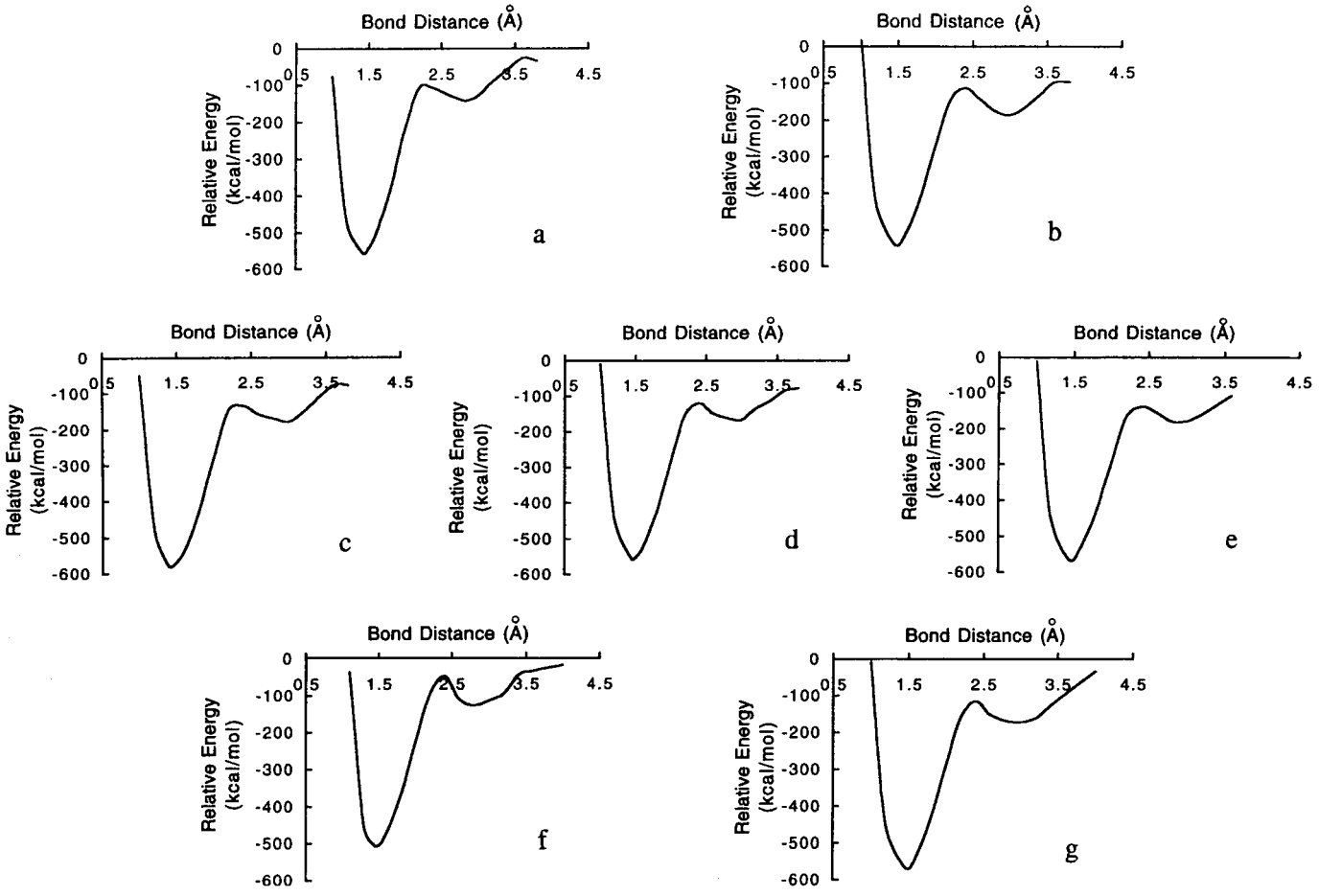

FIG. 12. Energy vs bond distance curves for different models (refer to Fig. 1): (a) $C_{14}H_7$, (b) $C_{14}H_7O$, (c) $C_{14}H_7OLi$, (d) $C_{14}H_7ONa$, (e) $C_{14}H_7OK$, (f) $C_{14}H_7OCa$, (g) $C_{14}H_7OCu$.

our graphite models were finite and the geometry parameters were not uniform for different bonds in the model. The *ab initio* results will be reported in terms of C–C bond energy before and after –O and –O–M groups were attached to the active carbon site.

Figure 12 shows the energy vs C–C bond distance curves for different models. Each curve has an energy minimum which corresponds to the C–C bond distance at the optimized length. The system energy is increased with the C–C bond distance away from the optimized position. When the bond length is further increased, the energy curve approaches a certain energy level which is the energy for the totally dissociated model. The difference between this energy level and the energy minimum was taken as the C–C bond energy for different models.

The C–C bond energies of different models are summarized in Table 2. In order to reduce the computational cost, not all of the 10 catalysts in this study were calculated. However, the models we chose for calculation were representative. They were (refer to Fig. 1): (i) the graphite model saturated with hydrogen; (ii) the graphite model with O atom attached to one of the active carbon, C_4; (iii) graphite models with –O–*M* group attached to C_4, where *M* stands for all the three alkali metals (Li, Na, and K) studied; one of the alkaline earth metals, Ca, which is next to K in the periodic table; and Cu, the most active transition metal catalyst in

TABLE 2

Calculated C–C Bond (C_3–C_4 and C_4–C_5, see Fig. 1) Energies for Different Models

Model	$C_{14}H_7$	$C_{14}H_7O$	$C_{14}H_7OLi$	$C_{14}H_7ONa$	$C_{14}H_7OK$	$C_{14}H_7OCa$	$C_{14}H_7OCu$
C–C BE	216.5	203.9	200.8	197.7	193.9	196.1	197.6

Note. The bond energies are in kcal/mol. The experimental C–C bond energy is about 170 kcal/mol.

this study. From the table, it is clear that the C–C bonds on the zigzag face were substantially weakened when an O atom was added to the active carbon site, C_4, and was further weakened by adding *M* to the O atom. As a consequence, the C–C bonds could be more easily broken for gasification to take place. One can see that the bond energies are very close, indicating that different elements do not have a large influence on the total bond energies of the C_4–C_3 and the C_4–C_5 bonds. This result is in agreement with the experimental fact that the gasification reactions catalyzed by all alkali elements showed very close activation energies (28, 29).

Comparing Tables 2 and 1, we can see that the relative order of the extent of the C–C bond weakening by different –O–*M* groups is in general agreement with the order of catalytic activity results from the TOF measurements; i.e., the more the C–C bond is weakened by the –O–*M* group, the more active *M* is in the catalytic channeling. Cu catalyst is an exception. As we can see from Table 2, the C–C bond energy with the –O–Cu group attached to the active carbon is 197.6 kcal/mol and it is not the smallest among the catalysts studied, but it showed the highest activity in catalytic channeling. There are a number of possible reasons for the disagreement on Cu; the small model size is one of them. Further calculations with larger models are needed to yield more accurate results.

NO–Graphite Reaction Mechanism

Based on electron microscopy observation and molecular orbital calculations, we have proposed a unified mechanism for all carbon gasification reactions by oxygen containing reactants (e.g., O_2, H_2O, CO_2, and NO) (11–13). The unified mechanism was based on semiempirical molecular orbital calculations and experimental results on alkali-catalyzed gasification reactions and was capable of explaining the kinetics of the $C + H_2O$ and $C + CO_2$ reactions catalyzed by alkali and alkaline earth catalysts.

From the proposed unified mechanism and from the STM and *ab initio* calculation results we have obtained in this study, the mechanism for the graphite–NO reaction,

$$C(\text{edge}) + 2NO \Leftrightarrow N_2O + C(O) \quad [1]$$

$$N_2O + C(\text{edge}) \Leftrightarrow N_2 + C(O) \quad [2]$$

$$N_2O + C(O) \rightarrow N_2 + CO_2 \quad [3]$$

$$C(O) \rightarrow CO, \quad [4]$$

is proposed, where C(edge) is the edge carbon site with a free sp^2 electron; i.e., C_4 in Fig. 1, C(O) represents the –C–O group shown in Fig. 1b. The first two steps are fast and the last two are slow and are hence rate determining.

ACKNOWLEDGMENT

This work was supported by the National Science Foundation Grant CTS-9523801.

REFERENCES

1. Marquez-Alvarez, C., Rodriguez-Ramos, I., and Guerrero-Ruiz, A., *Carbon* **34**, 339 (1996).
2. Illan-Gomez, M. J., Linares-Solano, A., Salinas-Martinez de Lecea, C., and Calo, J. M., *Energy Fuels* **7**, 146 (1993).
3. Yamashita, H., Yamada, H., and Tomita, A., *Appl. Catal.* **49**, 319 (1989).
4. Teng, H., Suuberg, E. M., and Calo, J. M., *Energy Fuels* **6**, 398 (1992).
5. Radovic, L. R., and Walker, P. L., Jr., *Fuel Proc. Technol.* **8**, 149 (1984).
6. Kapteijn, F., Mierop, A. J. C., Abbel, G., and Moulijn, J. A., *J. Chem. Soc. Chem. Commun.* 1085 (1984).
7. Inui, T., Otawa, T., and Takegami, Y., *Ind. Eng. Chem. Prod. Res. Dev.* **21**, 56 (1982).
8. Kakuta, N., Sumiya, S., and Yoshida, K., *Catal. Lett.* **11**, 71 (1991).
9. McKee, D. W., in "Chemistry and Physics of Carbon" (P. L. Walker, Jr., and P. A. Thrower, Eds.), Vol. 16. Dekker, New York, 1980.
10. Walker, P. L., Jr., Shelef, M., and Anderson, R. A., *in* "Chemistry and Physics of Carbon" (P. L. Walker, Jr., Ed.), Vol. 4, pp. 287. Dekker, New York, 1968.
11. Chen, S. G., and Yang, R. T., *J. Catal.* **141**, 102 (1993).
12. Chen, S. G., and Yang, R. T., *J. Catal.* **138**, 12 (1992).
13. Chen, S. G., and Yang, R. T., *Energy Fuels* **11**, 421 (1997).
14. Lee, G. W., *Coke and Gas* **23**, 398 (1961).
15. Patrick, J. W., and Shaw, F. H., *Fuel* **51**, 69 (1972).
16. Amariglio, H., and Duval, X., *Carbon* **4**, 323 (1966).
17. Pan, Z. J., and Yang, R. T., *J. Catal.* **130**, 161 (1991).
18. Goethel, P. J., and Yang, R. T., *J. Catal.* **119**, 201 (1989).
19. Goethel, P. J., and Yang, R. T., *J. Catal.* **111**, 220 (1988).
20. Goethel, P. J., and Yang, R. T., *J. Catal.* **108**, 356 (1987).
21. Goethel, P. J., and Yang, R. T., *J. Catal.* **101**, 342 (1986).
22. Yang, R. T., and Wong, C., *J. Catal.* **85**, 154 (1984).
23. Holstein, W. L., and Boudart, M., *J. Catal.* **75**, 337 (1982).
24. Radovic, L. R., Walker, P. L., Jr., and Jenkins, R. G., *J. Catal.* **82**, 382 (1983).
25. Mims, C. A., and Pabst, J. K., *J. Catal.* **107**, 209 (1987).
26. Moulijn, J. A., Cerfontain, M. B., and Kapteijn, F., *Fuel* **63**, 1043 (1984).
27. Chang, J., Lauderback, L. L., and Falconer, J. L., *Carbon* **29**, 645 (1991).
28. Kelemen, S. R., and Freund, H., *J. Catal.* **102**, 80 (1986).
29. Freund, H., *Fuel* **65**, 63 (1986).
30. Pereira, P., Csencsits, T., Somorjai, G. A., and Heinemann, H., *J. Catal.* **123**, 463 (1990).
31. Saber, J. M., Kester, K. B., Falconer, J. L., and Brown, L. F., *J. Catal.* **109**, 329 (1988).
32. Cerfontain, M. B., Meijer, R., Kapteijn, F., and Moulijn, J. A., *Carbon* **26**, 41 (1988).
33. Saber, J. M., Falconer, J. L., and Brown, L. F., *J. Catal.* **90**, 65 (1984).
34. Walker, P. L., Jr., Rusinko, F., Jr., and Austin, L. G., in "Advances in Catalysis" (D. D. Eley, P. W. Selwood, and P. B. Weisz, Eds.), Vol. 11, p. 133. Academic Press, New York, 1959.
35. Wen, W. Y., *Catal. Rev. Sci. Eng.* **22**, 1 (1980).
36. Yang, R. T., *in* "Chemistry and Physics of Carbon" (P. A. Thrower, Ed.), Vol. 19. Dekker, New York, 1984.
37. Wood, B. J., and Sancier, E. M., *Catal. Rev. Sci. Eng.* **26**, 233 (1984).
38. Baker, R. T. K., in "Carbon and Coal Gasification Science and Technology" (J. L. Figuereido and J. A. Moulijn, Eds.), NATO ASI Series E, No. 105, p. 231, Martinus Nijhoff, Dordrecht, 1986.
39. McKee, D. W., *Fuel* **62**, 170 (1983).
40. Veraa, M. J., and Bell, A. T., *Fuel* **57**, 194 (1978).
41. McKee, D. W., and Chatterji, S., *Carbon* **20**, 59 (1982).

42. Saber, J. M., Falconer, J. L., and Brown, L. F., *Fuel* **65**, 1356 (1986).
43. Mims, C. A., and Pabst, J. K., *Prepr. Div. Fuel Chem. Am. Chem. Soc.* **25**(3), 258 (1980).
44. Mims, C. A., and Pabst, J. K., in "Proceedings of the International Conference on Coal Science," p. 730. Verlag Gluckauf, Essen, 1981.
45. Freriks, I. L. C., Van Wechem, H. M. H., and Stuiver, J. C. M., *Fuel* **60**, 463 (1981).
46. Mims, C. A., Rose, K. D., Memchior, M. T., and Pabst, J. K., *J. Am. Chem. Soc.* **104**, 6887 (1982).
47. Yuh, S. J., and Wolf, E. E., *Fuel* **62**, 252 (1983).
48. Delannay, F., Tysoe, W. T., Heinemann, H., and Somorjai, G. A., *Carbon* **22**, 401 (1984).
49. Meijer, R., Weeda, M., Kapteijn, F., and Moulijn, J. A., *Carbon* **29**, 929 (1991).
50. Baker, R. T. K., *Catal. Rev. Sci. Eng.* **19**(2), 161 (1979).
51. Hashimoto, H., Naiki, T., Eto, T., and Fujwara, K., *Jpn. J. Appl. Phys.* **7**, 946 (1968).
52. Baker, R. T. K., and Harris, P. S., *J. Phys. E.* **5**, 793 (1970).
53. Hennig, G., *J. Inorg. Nucl. Chem.* **24**, 1129 (1962).
54. Hennig, G. R., *J. Chem. Phys.* **40**, 2877 (1964).
55. Evans, E. L., Griffiths, R. J. M., and Thomas, J. M., *Science* **171**, 174 (1971).
56. Thomas, J. M., *in* "Chemistry and Physics of Carbon" (P. L. Walker, Jr., Ed.), Vol. 1. Dekker, New York, 1965.
57. Harris, P. S., Feates, F. S., and Reuben, B. G., *Carbon* **11**, 565 (1973).
58. Baker, R. T. K., *Carbon* **24**, 715 (1986).
59. Baker, R. T. K., Lund, C. R. F., and Chludzinski, J. J., Jr., *J. Catal.* **87**, 255 (1984).
60. Fulghum, J. E., McGuire, G. E., Musselman, I. H., Nemanich, R. J., White, J. M., Chopra, D. R., and Chourasia, A. R., *Anal. Chem.* **61**, 243R (1989).
61. Kuk, Y., and Silverman, P. J., *Rev. Sci. Instrum.* **60**, 165 (1989).
62. Chang, H., and Bard, A., *J. Am. Chem. Soc.* **112**, 4598 (1990).
63. Chang, H., and Bard, A., *J. Am. Chem. Soc.* **113**, 5588 (1991).
64. Chu, X., Schmidt, L. D., Chen, S. G., and Yang, R. T., *J. Catal.* **140**, 543 (1993).
65. Chu, X., and Schmidt, L. D., *Ind. Eng. Chem. Res.* **32**, 1359 (1993).
66. Chu, X., Schmidt, L. D., *Carbon* **29**, 1251 (1991).
67. Miranda, R., Garcia, N., Baro, A. M., Garcia, R., Pena, J. L., and Rohrer, H., *Appl. Phys. Lett.* **47**, 367 (1985).
68. Gimzeski, J. K., and Humbert, A., *IBM J. Res. Develop.* **30**, 472 (1986).
69. Bennett, A. L., McCarroll, B., and Messmer, R. P., *Phys. Rev. B* **3**, 1397 (1971).
70. Hayns, M. R., *Theoret. Chim. Acta* (Berlin) **39**, 61 (1975).
71. Chen, J. P., and Yang, R. T., *Surf. Sci.* **216**, 481 (1989).
72. Pan, Z. J., and Yang, R. T., *J. Catal.* **123**, 206 (1990).
73. Frisch, M. J., Trucks, G. W., Schlegel, H. B., Gill, P. M. W., Johnson, B. G., Robs, M. A., Cheeseman, J. R., Keith, T., Petersson, G. A., Montgomery, J. A., Raghavachari, K., Al-Laham, M. A., Zakrzewski, V. G., Ortiz, J. V., Foresman, J. B., Peng, C. Y., Ayala, P. Y., Chen, W., Wong, M. W., Andres, J. L., Replogle, E. S., Gomperts, R., Martin, R. L., Fox, D. J., Binkley, J. S., DeFrees, D. J., Baker, J., Stewart, J. P., Head-Gordon, M., Gonzalez, G., and Pople, J. A., *Gaussian 94 Revision B* **3** (Gaussian, Inc., Pittsburgh, 1995).
74. Moore, A. W., *in* "Chemistry and Physics of Carbon," Vol. 17, Dekker, New York, 1981.
75. Keep, C. W., Terry, S., and Wells, M., *J. Catal.* **66**, 451 (1980).
76. Chen, N., Yang, R. T., and Goldman, R. S., *J. Catal.*
77. Baker, R. T. K., France, J. A., Rouse, L., and Waite, R. J., *J. Catal.* **41**, 22 (1976).